ACCOUNTS
of chemical research

Direct Comparison of Kinetic and Thermodynamic Influences on Gold Nanomorphology

AMANDA S. BARNARD*
CSIRO Materials Science and Engineering, Parkville, VIC 3052, Australia

RECEIVED ON JANUARY 16, 2012

CONSPECTUS

Under a given set of conditions, nanomaterials can crystallize into structures that are entirely inconsistent with the bulk material and may adopt a range of faceted morphologies that depend on the particle size. A size-dependent phase diagram, a graphical representation of the chemical equilibrium, offers a convenient way to describe this relationship among the size, morphology, and thermodynamic environment. Although creating such a diagram from conventional experiments is extremely challenging (and costly), theory and simulation allow us to use virtual experiments to control the temperature, pressure, size, structure and composition independently.

Although the stability and morphology of gold nanoparticles has been addressed numerous times in recent years, a critical examination of the literature reveals a number of glaring contradictions. Typically gold nanoparticles present as multiply-twinned structures, such as icosahedra and decahedra, or faceted monocrystalline (fcc) shapes, such as truncated octahedra and cuboctahedra. All of these shapes are dominated by various fractions of {111} and {100} facets, which have different surface atom densities, electronic structure, bonding, chemical reactivities, and thermodynamic properties. Although many of the computational (and theoretical) studies agree on the energetic order of the different motifs and shapes, they do not necessarily agree with experimental observations. When discrepancies arise between experimental observations and thermodynamic modeling, they are often attributed to kinetics. But only recently could researchers analytically compare the kinetics and thermodynamics of faceted nanoparticles.

In this Account, we follow a theoretical study of the size, shape, and structure of nanogold. We systematically explore why certain shapes are expected at different sizes and (more importantly) why others are actually observed. Icosahedra are only thermodynamically preferred at small sizes, but we find that they are the most frequently observed structures at larger sizes because they are kinetically stable (and coarsen more rapidly). In contrast, although the phase diagram correctly predicts that other motifs will emerge at larger sizes, it overestimates the frequency of those observations. These results suggest either a competition or collaboration between the kinetic and thermodynamic influences.

We can understand this interaction between influences if we consider the change in shape and the change in size over time. We then use the outputs of the kinetic model as inputs for the thermodynamic model to plot the thermodynamic stability as a function of time. This comparison confirms that decahedra emerge through a combination of kinetics and thermodynamics, and that the fcc shapes are repressed due to an energetic penalty associated with the significant departure from the thermodynamically preferred shape. The infrequent observation of the fcc structures is governed by thermodynamics alone.

Introduction

Although nanomaterials design is the focus of considerable research, controlling nanoscale features is still challenging, and dramatic changes in fundamental properties may result from modest variations in the size or shape. Structural changes can also be driven or invoked spontaneously by changes in the local environment. For this reason, a complete understanding of the structural stability of any nanomaterial, with respect to its physical and chemical environment, is essential to ensure uniformity and reliability for our future technologies.

While it is well-known that many materials can adopt a variety of different polymorphs, depending upon the thermodynamic conditions, under the same environment

Published on the Web 06/15/2012 www.pubs.acs.org/accounts
10.1021/ar3000184

many nanomaterials may crystallize in structures that are entirely inconsistent with the bulk. This can occur in multicomponent or homoelemental materials, each with a characteristic size at which the new or alternative structures emerge. This critical crossover size is unique for a particular material, is intrinsic to the structures that are being compared, and (as mentioned above) may shift in response to changes in the thermodynamic conditions. In some cases, the structural change may not involve the transformation to another polymorph, but may be more subtle, involving only a morphological transformation to a different motif or shape.

A convenient way of describing the relationship between different structures as a function of size and environment is to create a nanoscale phase diagram, which is a graphical representation of chemical equilibrium. Typically one axis represents the temperature (*T*), composition (*C*), or pressure (*P*), and the other represents the number of atoms (*N*) or average diameter (*D*). When the crystal structure remains constant but the external shape (habit) of the crystal changes, then phase diagrams give way to morphology maps, but the principle remains the same. These size-dependent shape and phase relationships may be explored by analyzing the specific free energy and enthalpy of formation, which is ideally done using theory and simulation. Using *virtual experiments*, one can control the phase, shape, size, composition, temperature, and pressure independently, and systematically include regions on a phase diagram for different crystalline polymorphs, motifs, and melts. This is extremely challenging (and costly) to do using conventional experiments, particularly when one is dealing with expensive commodities such as noble metals.

Among the variety of noble metal nanoparticles produced today, gold is perhaps the most studied, due to a number of desirable properties.[1] Many of these properties are strongly linked with the nanomorphology, and the relationship between properties (and ultimately, applications) and the physical structure is central to the chemistry[2−5] and biochemistry[6] of nanogold. These structure/property relationships have been the focus of numerous studies,[7] and considerable effort is being directed to understanding how engineering the size and shape of nanogold can improve performance.[8−10] In general, biomedical applications of nanogold are particularly important, including diagnostics applications such as visualization and bioimaging, analytical methods, and plasmonic biosensors; therapeutic applications such as photothermal therapy, photodynamic therapy, and drug and gene delivery; and immunological applications and the study of biodistribution and toxicity.[11]

Typically gold nanoparticles present as icosahedra and truncated icosahedra,[12,13] decahedra and truncated decahedra,[13,14] truncated octahedra and cuboctahedra (or variants of these shapes),[15−17] or singly or multiply twinned face-centered cubic (fcc) structures.[12,18] All of these shapes are dominated by various fractions of {111} and {100} facets, which have different surface atom densities, electronic structure, bonding, chemical reactivities, and thermodynamic properties. Both decahedra and icosahedra are based on fcc units separated by ⟨111⟩ twin planes. Although the stability and nanomorphology has been addressed numerous times over the years, a critical examination of the literature reveals a number of contradictions. While many of the computational (and theoretical) studies agree on the energetic order of different motifs and shapes, they do not necessarily agree with experimental observations. When discrepancies arise between experimental observations and thermodynamic modeling, they are often attributed to kinetics. Similarly, when discrepancies arise between experimental observations and kinetic modeling and simulation, they are often attributed to thermodynamics.

These "default" attributions are assigned by a process of elimination and often remain untested, because rigorous validation requires a way of directly comparing kinetics and thermodynamics of an enormous range of faceted nanoparticles (based on a consistent set of input parameters), which has not been possible in the past.[19] However, due to the development of a number of complementary techniques, this comparison is now possible. In this Account, we follow a theoretical study of the size, shape, and structure of nanogold that systematically explores why certain shapes are expected at different sizes and (most importantly) why others are actually observed.

Thermodynamic Modeling and Stability

In the past, the modeling of nanogold has been based almost exclusively on energetic considerations. In most cases, the aim as been to determine the correct energetic ordering of different motifs and to identify the sizes at which morphological transformation may be expected.

Small Nanoparticles and Clusters. To build a general description of nanogold, it is convenient to start at the bottom, where theoretical and computational studies have been reported that have provided valuable information on size, structure, and energetics, over a wide range of sizes from only a few atoms up to 3 nm. Pyykkö[20,21] has published detailed reviews of many theoretical studies that included a comprehensive survey of calculations on neutral and charged gold clusters, highlighting the rich range of possible

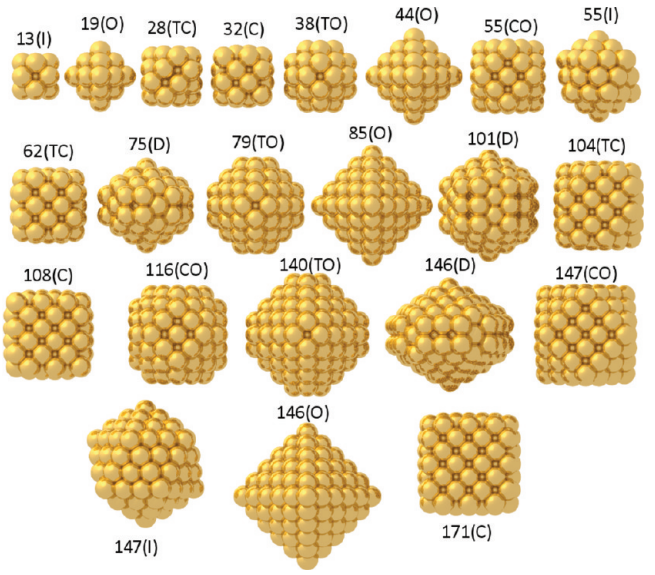

FIGURE 1. The 22 gold nanoparticle structures examined using relativistic DFT by Barnard and Curtiss.[31] *N*(X) denotes the size and shape, where *N* is the numbers of atoms, I = icosahedron, O = octahedron, TO = truncated octahedron, CO = cuboctahedron, TC = truncated cube, C = cube, and D = decahedron.

structures. As determined by a variety of computational methods, the equilibrium structures over 1 nm in size include fcc single crystals,[15] singly- or multiply twinned fcc structures,[18] twinned hexagonal close-packed (hcp) structures,[22] icosahedra, truncated icosahedra, and truncated decahedra. The majority of computational studies in this size range have focused on characterizing the icosahedral and decahedral particles,[24,25] and the crossover among these structural motifs has also been explicitly examined.[26]

Because it has been firmly established that relativistic effects are an essential part of the *ab initio* modeling of nanogold,[4,20] a systematic relativistic DFT study was undertaken in 2006,[31] including the variety of (fully relaxed) sizes and shapes, as shown in Figure 1. In this study, the size- and shape-dependent features were explored, including simple trends in the length of the bonds between atoms (compared with bulk gold) and detailed information on surface reconstructions and lattice distortions. Predictions of the variations in average bond length with particle size were consistent with other computational studies[27−29] and were in good qualitative agreement with experimental high-resolution electron diffraction (HREM) and X-ray diffraction (XRD) results.[16] In addition to the structural properties, the potential energies of the 22 shapes and motifs were plotted as a function $N^{1/3}$, to establish the energetic ordering of the shapes at small sizes (see Figure 2a).

In order to construct a viable framework for extrapolation, the results were replotted as a function of the average coordination of the nanoparticle (see Figure 2b), because this is very sensitive to the shape of the particle (and to the motif) and is proportional to the surface-to-volume ratio (which is an indicator of both size and shape). These extrapolations predicted that the truncated octahedron is energetically preferred at large sizes, followed by the octahedron, truncated cube, and finally the cuboctahedron; in agreement with the electron microscopy studies of fcc gold nanoparticles.[16,30] However, one must question the validity of extrapolations when the sample set is restricted to a maximum size <200 atoms yet aims to predict the stability of nanoparticles with >10 000 atoms. To make such predictions, there are alternative methods (also based on relativistic simulations) that are more appropriate.

Nanocrystals and Quasicrystals. One appropriate method is called *thermodynamic cartography*, which is literally a mapping of the thermodynamically preferred structure (size, phase, polymorph, motif, or shape) in a space defined by a range of different physical parameters. These parameters may include (but are not restricted to) thermodynamic factors such as temperature, pressure, and different measures of the chemical environment. In the absence of a substrate or support, this may be done using a simple shape-dependent thermodynamic model similar to a Wulff construction.[32] The model is based on a geometric summation of the specific Gibbs free energy $G(T)$ of an entire nanoparticle and includes the important phenomenological features such as the bulk, surfaces, and twins:

$$G(T) = \Delta G_f^\circ(T) + \frac{M}{\rho}\left(1 - \frac{2\sum_i f_i\sigma_i(T)}{B_0\langle R\rangle} + \frac{P_{ex}}{B_0}\right)\left[q\sum_i f_i\gamma_i(T) + n\sum_\theta\left(a_\theta\nu_\theta(T) + \sum_\phi l_{\theta\phi}\eta_\phi(T)\right)\right] \quad (1)$$

where M is the molar mass, ρ is the mass density, $\gamma_i(T)$ is the temperature-dependent free energy of facet i, $\nu_\theta(T)$ is the energy of the twin plane of area a in orientation θ, and $\eta_\phi(T)$ is the re-entrant line tension where the twin plane intersects with the free surface in the orientation ϕ, with length l. Dimensional consistency is preserved by introducing the number density of planar defects $n = n_t/V$ (where n_t is the total number of defects and V is the total volume). In this model f_i is a weighting factor that defines the fractional surfaces areas, such that $\sum_i f_i = 1$. This model also accounts for the elastic effects of surface stress. The volume dilation induced by the isotropic surface stresses σ_i and external pressure P_{ex} is included using the Laplace−Young formalism using the bulk modulus B_0, and the

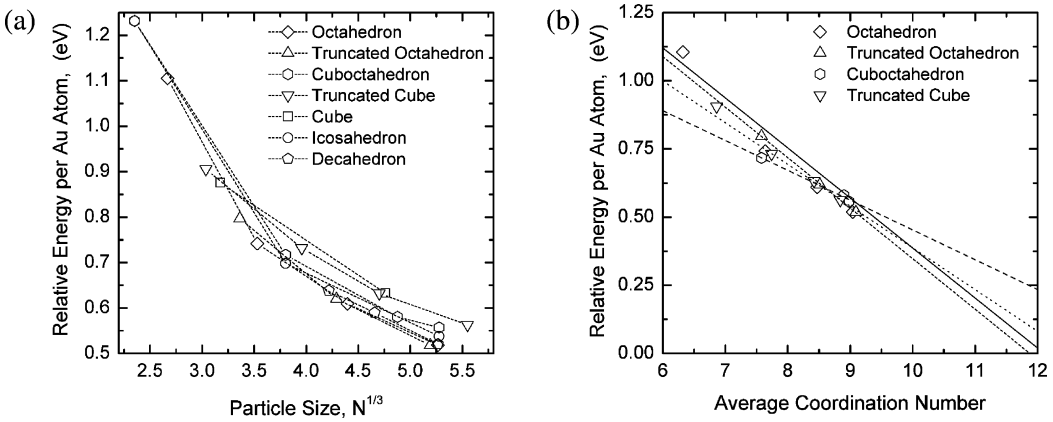

FIGURE 2. The energy of the gold nanoparticles shown in Figure 1, as a function of (a) the number volume, $N^{1/3}$, and (b) the average Au−Au coordination number. Reproduced with permission from ref 31. Copyright 2006 Wiley-VCH Verlag GmbH & Co. KGaA.

average particle radius $\langle R \rangle$ calculated using a spherical approximation. In the following sections, atmospheric external pressure has been assumed ($P_{ex} = 101.33$ kPa).

This version of the model requires the input of B_0, $\gamma_i(T)$, $\sigma_i(T)$, $\nu_\theta(T)$, and $\eta_\phi(T)$, which must be calculated explicitly for all facets i, θ, and ϕ of interest, using (the same) appropriate computational method. In this case, relativistic DFT has been used,[34] with the same input settings and convergence criteria that were used for the small isolated particles described above.[31] If one were so inclined, this is where additional complexity can be introduced, such as variations in surface chemistry or surface charge. In general, the geometric parameters $\langle R \rangle$, q, f_i, n, a_θ, and $l_{\theta,\phi}$ provide the size and shape dependence, and defining these parameters can be complicated, depending upon the shapes in question. More information on how to calculate q and f_i for fcc structures is provided in ref 33.

Shown in Figure 3 is an example of the type of results that can be generated using this technique, comparing the relative stability of the shapes displayed in Figure 4 as a function of average particle size. The crossovers in this graph indicate the transformation sizes between pairs of structures and can be used to generate a phase map once the temperature dependence of these points is known. Since the DFT input parameters were calculated at $T \approx 0$ K, a number of simple expressions must be introduced to describe the temperature dependence,[35] such as the semiempirical expression:

$$\gamma_i(T) = \gamma_i(0)\left(1 - \frac{T}{T_{ci}}\right)^x \qquad (2)$$

where x is an empirical parameter (known to be unity for metals[36]) and T_c is the critical temperature at which

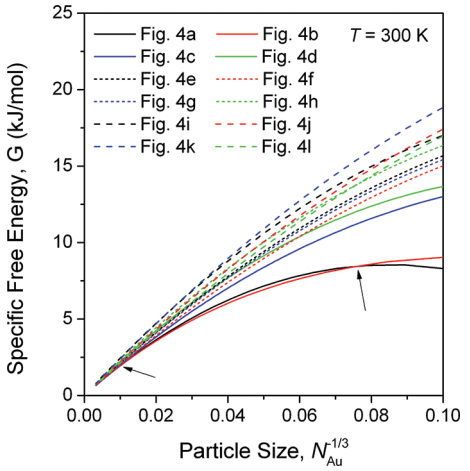

FIGURE 3. For each shape in Figure 4, the specific free energy is shown at room temperature.

the surface structure deteriorates or changes significantly from the bulk structure. T_c is usually taken as the bulk surface melting temperature, which is size-dependent and may easily be calculated using the expression of Qi and Wang:[37]

$$T_{ci} = T_{mi}\left(1 - \frac{6r\Omega}{\langle D \rangle}\right) = T_{mi}(1 - qr) \qquad (3)$$

where T_{mi} is the macroscopic surface melting temperature of facet i, $\langle D \rangle$ is the average particle diameter, r is the atomic radius, and Ω is a shape-dependent factor defined as the surface area of the nanoparticle divided by the surface area of a sphere of equivalent volume.[37] This reduces to a function of the surface-to-volume ratio q, which is the same value as in eq 1, which creates a feedback loop during any shape optimization.[38] The optimization of the nanoparticle shape at a given temperature

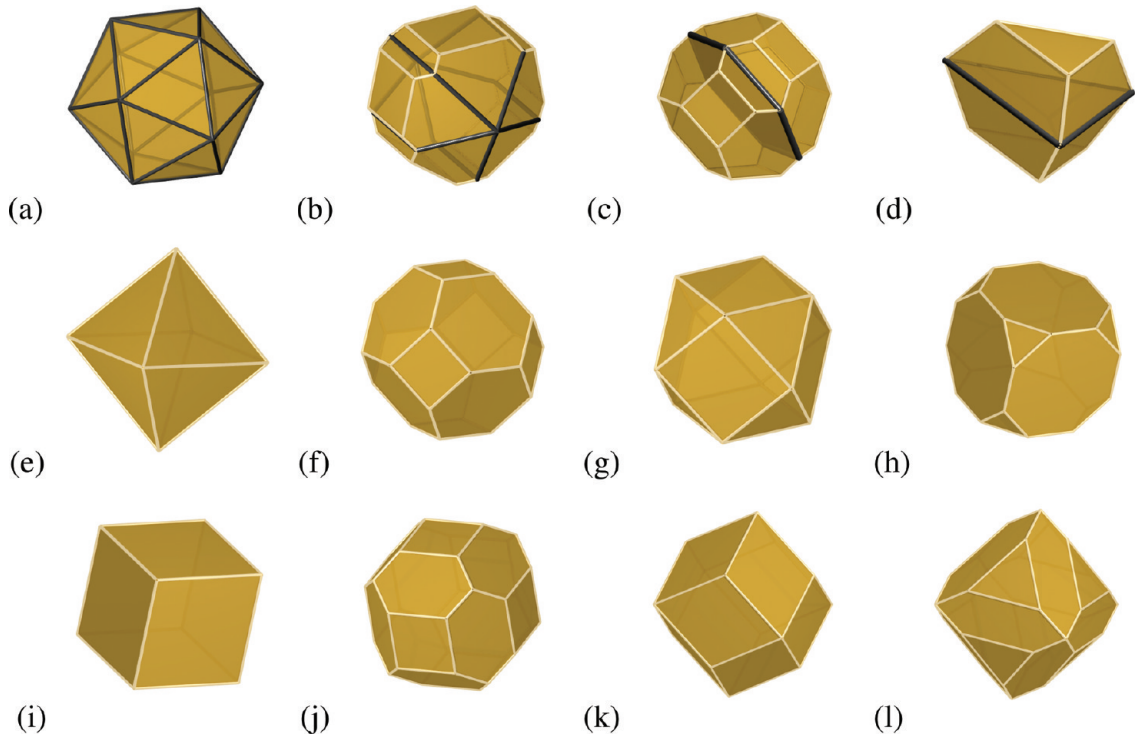

FIGURE 4. Possible morphologies of nanogold, including the (a) icosahedron, (b) decahedron, (c) twinned truncated octahedron, (d) trigon, (e) octahedron, (f) truncated octahedron, (g) cuboctahedron, (h) truncated cube, (i) cube, (j) cubo-truncated rhombic dodecahedron, (k) rhombic dodecahedron, and (l) octo-truncated rhombic dodecahedron.

will change T_{ci}, which then affects the temperature dependence in eq 2, which then in turn further alters the shape. Since $\sigma = \gamma + A\partial\gamma/\partial A$ the temperature dependence of σ_i may be described in the same way.

Nanogold Phase Diagram. Using the models and methods described above the temperature-dependent specific Gibbs free energy of formation of each motif may be predicted. By repeating the comparison in Figure 3 at different sizes and temperatures, one can map the crossovers in $\langle N,T \rangle$ space, and by adding a description of the size-dependent melting of the entire nanoparticle, one can extend this morphology map to provide a complete nanoscale phase diagram of gold. Like many materials, at elevated temperature, the melting point of gold decreases with size, and this can be modeled using eq 3 with $T_{ci} \rightarrow T_{m,nano}$ and $T_{mi} \rightarrow T_{m,bulk}$. The thermodynamic analysis of size-dependent melting was discussed as early as 1909[39] and established experimentally for gold in the classic work of Buffat and Borel in 1976.[40] Combining these results gives a quantitative phase diagram of nanogold, based on relativistic first principles calculations[41] (see Figure 5), in agreement with previous selective studies examining their stability at different sizes.[26]

Readers will note that this phase diagram predicts the onset of different types of melting behavior, below the

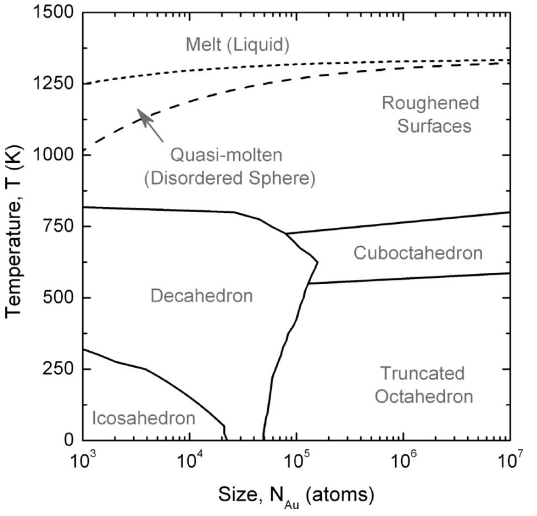

FIGURE 5. Phase diagram of nanogold, based on relativistic first principles calculations. Reproduced with permission from ref 41. Copyright 2009 American Chemical Society.

solid–liquid transformation at high temperature (in agreement with experiment[43]). This includes a "quasi-molten" region observed by others,[23,42] where decahedral and fcc particles will be sufficiently fluid so as to adopt the icosahedral motif (before melting). Beneath the quasi-molten region, "surface roughening" occurs when the surface structure

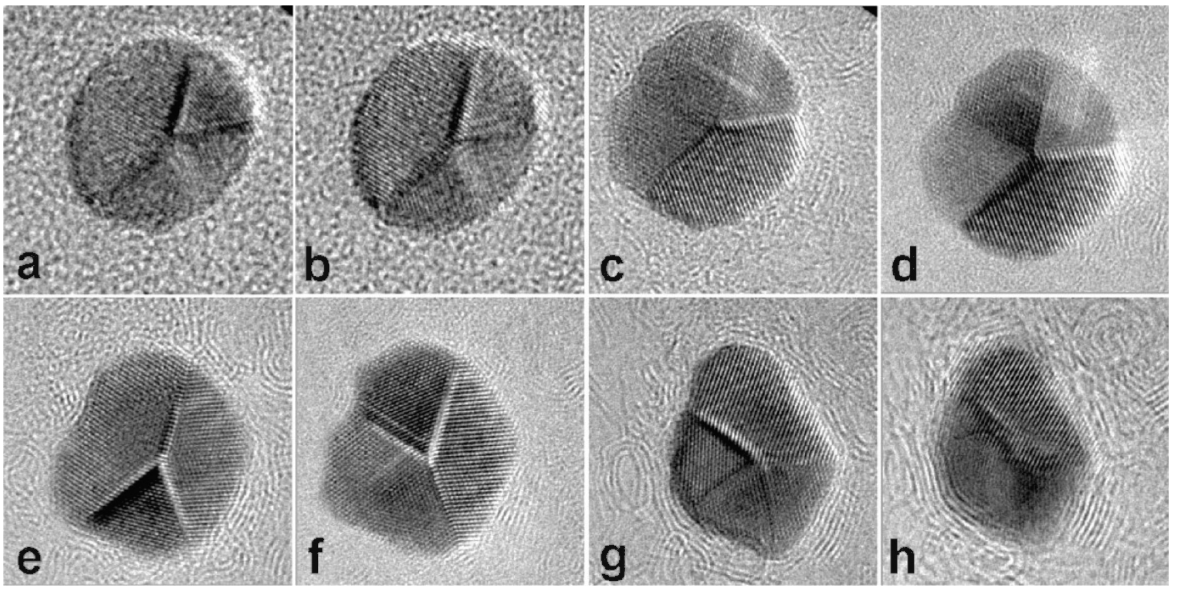

FIGURE 6. Representative images taken from a series of HRTEM images of a ~10.3 nm Au nanoparticle as a function of temperature. Initial decahedral structure (close to a ⟨110⟩ projection) at (a) 300 (room temperature), (b) 600, (c) 750, and (d) 800 K. (e,f) At 900 K, the structure becomes distorted, with significant surface roughening, but retains the underlying crystallinity; (g) 950 and (h) 1000 K, crystalline areas are still apparent, though the surface appears almost fluid. Reproduced with permission from ref 41. Copyright 2009 American Chemical Society.

deteriorates but the crystallinity of the core is preserved. This feature was a direct consequence of the theoretical description of the critical temperature,[37] which includes size-dependent surface melting. As the temperature is increased, the surface melting temperature is surpassed before the corresponding bulk melting temperature is attained.

To verify this phase diagram, colloidal gold nanoparticles ranging from 5−12 nm were prepared by reduction of dilute solutions of tetrachloroauric acid, using maltodextrin to prevent aggregation. The individual nanoparticles were examined using high-resolution aberration corrected transmission electron microscopy (HRTEM) to assign their structure. The samples were equilibrated via steady heating in the TEM, from room temperature up to ~700 K, during which the morphology of individual particles was clearly recognizable in projection. A statistical analysis of samples surviving the heating experiment reveals that 88% of the (equilibrated) nanoparticles exhibited the decahedral structure after heating to 650−700 K, while 12% retained the as-grown (mainly icosahedral) structure. Following equilibration, the decahedral/surface roughening transformation line was interrogated by heating equilibrated nanoparticles to between ~800 and ~850 K. Upon reheating, the core crystallinity was found to be resilient, although the surfaces become ill-defined. A temperature sequence illustrating typical results is given in Figure 6, showing a single 10.3 nm gold nanoparticle heated to above the roughening temperature. This observation is typical of surface roughening and through repeated experiments was sufficient to validate the theory.

Kinetic Modeling and Growth

Although this phase diagram was rigorously validated, its predictions are inconsistent with numerous experimental observations. During the detailed population study carried out by Koga and Sugawara[44] using high-resolution electron microscopy on over 4000 individual gold nanoparticles (ranging 3−18 nm, grown by an inert gas aggregation source in helium), it was found that icosahedra dominated the entire size range, even though they are not thermodynamically stable over ~4 nm at room temperature (see Figure 7). Decahedra were the next most prevalent, though the morphology was found to be more "flattened" than the traditional Marks decahedron that is normally assumed. This, together with the lack of untwinned fcc shapes, suggests that nonthermodynamic influences are at work.

Nuclei and Formation. To understand how nanogold is formed, we return our attention to small clusters and nuclei. Modeling of nucleation involves a number of approximations,[45−47] but it is possible to investigate the structure of nuclei using computer simulations. For example, Grochola et al.[48] used a classical EAM potential to simulate the nucleation of gold nanoparticles in the vapor. By repeating the simulations under a range of conditions, they showed

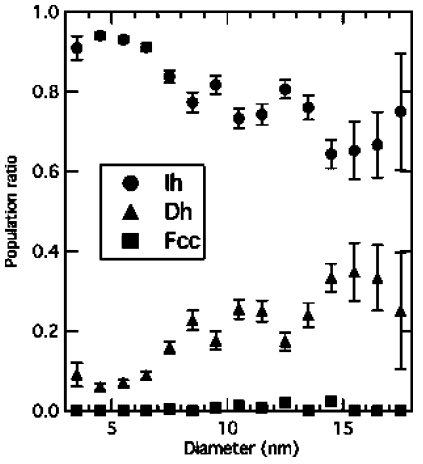

FIGURE 7. The population distributions of icosahedral (Ih), decahedral (Dh), and fcc morphologies (shape not specified) as a function of size. Error bars indicate the statistical error on the data. Reproduced with permission from ref 44. Copyright 2003 Elsevier.

that lower temperatures are mainly responsible for the occurrence of the decahedral and fcc nuclei, while "ideal" atom-by-atom growth conditions almost exclusively produced icosahedra.[48] Using both hybrid Monte Carlo and MD simulations, Desgranges and Delhommelle undertook a study of the nucleation of nanogold from a supercooled liquid and showed that although the structure of the nucleus is dominated by stable fcc structures in the early stages of nucleation, metastable hcp structures nucleate heterogeneously on the surface when the size approaches the critical diameter. The growth of the crystallite was also found to proceed through successive cross-nucleations between the two polymorphs.[49]

Following nucleation nanoparticles grow via a number of mechanisms, the most dominant of which (at least in the early stage) is coarsening. Often referred to as *kinetic growth* (or just plain "growth") this process involves the deposition of successive crystal layers due to the adsorption of monomers from a surrounding reservoir. This process may be studied computationally by constructing a model system and allowing the system to evolve subject to some known constraints.[19] Using the MD method mentioned above, Grochola et al. also studied the coarsening of nanogold in the vapor phase.[48] The final morphologies ~5 nm in diameter were identified via visual inspection and included (in order of occurrence frequency) icosahedra, simple decahedra, truncated triangular bipyramids, and fcc truncated octahedra. Irrespective of the monomer introduction rate or temperature, icosahedra were by far the most dominant shape at these sizes (around 3000 atoms).

Evolution and Coarsening. An alternative way of modeling the growth of nanogold is to use an analytical model that traces the evolution of different shapes as a function of time. One example is the surface area limited (SAL) model,[50] designed specifically for the kinetic modeling of nanomorphology. It is based on classical theories[51−53] but, unlike the predecessors, goes beyond the spherical approximation and enables one to explore the evolution of faceted shapes. This is achieved by devolving the coarsening of the entire nanoparticle into a sum of the coarsening of individual facets (i) with a limited area, described by the velocity of the growth front, dL_i/dt:

$$\frac{dL_i}{dt} = \frac{-V_m X d}{N_{\mathrm{eff},i}} \left(\frac{\nu \exp\left[\frac{-E_{\mathrm{diff},i}}{k_B T}\right] k_B T \ln\left[\frac{C_{eq}(t)}{C_0(t)}\right]}{\exp\left[\frac{E_{\mathrm{ad},i} - E_{\mathrm{des},i}}{2k_B T}\right]} \right) \quad (4)$$

where k_B is Boltzmann's constant, T is the absolute temperature, t is time, V_m is the molar volume of the monomer, X is the number of monolayers present, each of thickness d (where d is defined by the lattice parameters of the crystal), and ν is the sum of the vibrational (and possibly rotational) frequencies of the monomer on the surface. E_{diff} is the activation energy required for diffusion, E_{ad} and E_{des} are the activation energies of adsorption and desorption, and C_0(t) and C_{eq}(t) are the concentrations of the reservoir and the concentration of monomers participating in the coarsening monolayer, respectively. Together C_0(t) and C_{eq}(t) comprise the chemical potential gradient that ultimately drives the growth.

In this model, much of the shape dependence is introduced by $N_{\mathrm{eff},i}$, which is the effective number of sites available for monomers to adsorb and possibly diffuse. As described in ref 50, $N_{\mathrm{eff},i}$ is partially determined by the crystal structure, the shape and orientation of the individual (unique) facet i, and the finite size of the facet at a given point in time, beginning with the size (and shape) of the initial "seed". Under diffusion-limited conditions, monolayers are deposited on the facets of the seed due to the driving force provided by the chemical potential gradient (which is negative). Under reaction-limited conditions (when the chemical potential gradient is positive), deposited material desorbs, returning the monomers to the reservoir and ultimately recovering the initial seed. To model unrestricted growth on all facets simultaneously, eq 4 must be solved self-consistently, since the addition of a monolayer on facet i may also alter the size (and possibly the shape) of the alternative facet j. After each time step, the value of $N_{\mathrm{eff},i}(t)$ must be re-evaluated and $N_{\mathrm{eff},i}(t+1)$ and $N_{\mathrm{eff},j}(t+1)$ updated accordingly.

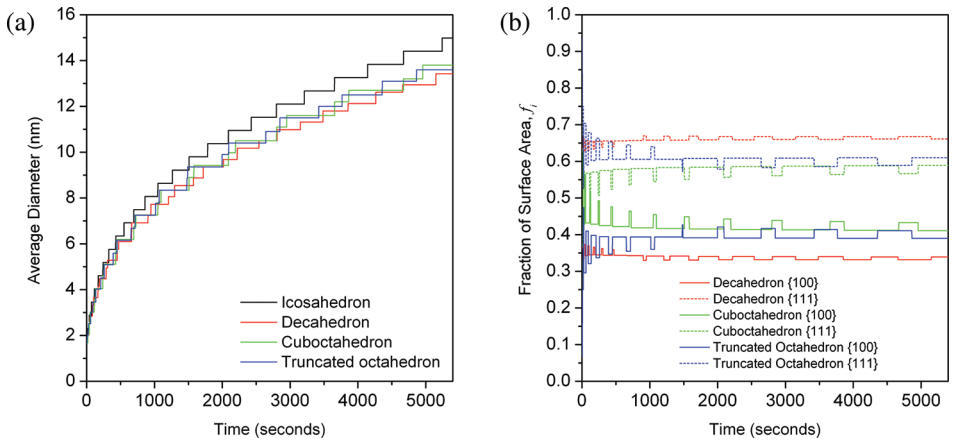

FIGURE 8. (a) Size-dependent and (b) shape-dependent evolution of gold nanoparticles from a 1.7 nm seed at $T = 298.15$ K and $C_0 = 1$ mol.

This model is conveniently based on a limited set of physical and chemical parameters that may be computed using DFT. It requires the input of the adsorption/desorption and diffusion energies and the appropriate selection (or variations) in $C_{eq}(t)$, N_{eff}, $C_0(t)$, and T, and will output the size and relative fraction of different facet areas at a given time, t. In this case, the values of the materials parameters are reported in ref 50 and are computationally consistent with the material parameters used in the thermodynamic model.

Previous testing[54] determined that small seeds give rise to a more rapid coarsening rate at the early stages of growth, but the later steady-state growth is unaffected by seed size. Changing the initial seed size has little impact on the final size, but can have considerable impact on the shape of the fcc structures. In contrast, temperature has a significant affect on particle size. Coarsening becomes more rapid during the steady-state period as the temperature is raised, so the particles are generally larger at a give time t. Increasing the availability of growth material (C_0) has a similar effect, and lowering the concentration of the reservoir slows growth. As the concentration of the reservoir diminishes and the relative concentration at the surface increases (as the monomers are deposited), the chemical potential gradient approaches one, and the size begins to converge. Eventually all of the growth material is adsorbed and coarsening will cease all together. Even though this is likely to occur at different times on different facets, the relative fraction of surface areas is almost unaffected, indicating that the shape evolution is practically independent of C_0 and T. Shape selectivity is primarily governed by the crystallography of the system.

The evolution of the different shapes is shown in Figure 8, beginning with a ~1.7 nm seed, $C_0 = 1$ kJ/mol, and $T = 298.15$ K. The individual steps along the curves represent the formation of individual monolayers on either the {111} or {100} facets. As time progresses, the facets area increases, and the monolayers take longer to fill. The steady-state coarsening of the truncated octahedron, cuboctahedron, and decahedron all exhibit fluctuations since the deposition of monolayers on the {111} or {100} facets changes the shape of the alternative facets (as well as the size). Over long time periods, the cuboctahedron and the truncated octahedron converge to the same shape, with 66% {111} and 34% {100} surface area. The decahedron increases the fraction of {111} surface area, making it more "pancake-like", in agreement with experiment.[44]

Combining and Correlating Kinetic and Thermodynamic Results

It is clear from the kinetic modeling that the icosahedron is most frequently observed because it is kinetically stable, but other motifs are still observed in experiments. The phase diagram (obtained using the thermodynamic model) predicts that other motifs will emerge at larger sizes, even though they coarsen more slowly, but with far greater frequency than they are actually seen. This suggests either a competition or collaboration between the kinetic and thermodynamic influences.

To understand this relationship, we recognize that the outputs of the kinetic model (the size and fraction of different surface facets) provide the ideal inputs for the thermodynamic model (q, $\langle R \rangle$, and f_i) and that all the input parameters were calculated using the same computational approach. We may therefore calculate the free energy of the kinetic shapes and effectively plot the thermodynamic stability as a function of time, $G(t)$. In Figure 9a, we see $G(t)$ for each of the candidate structures. At first the icosahedron is both kinetically and thermodynamically stable, but when the particles

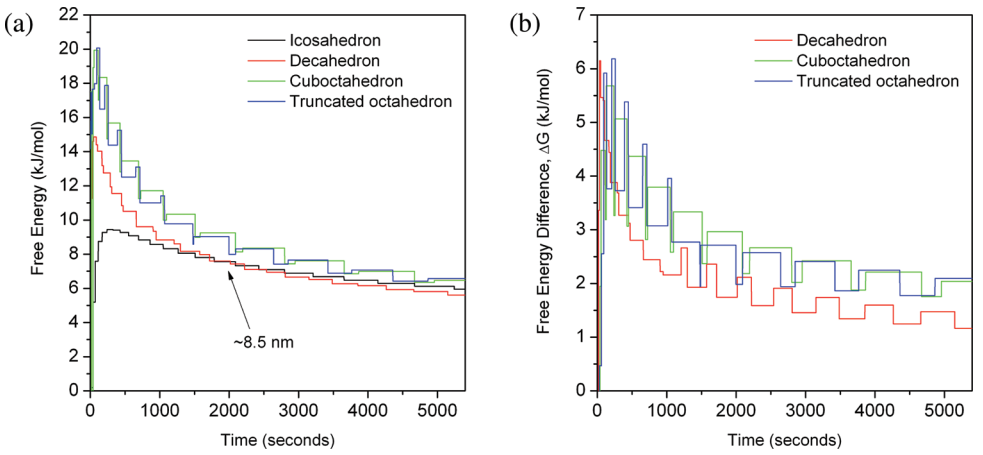

FIGURE 9. (a) Thermodynamic free energy of nanogold at the size and shape described in Figure 8 and (b) a direct comparison with the thermodynamically ideal shape from Figure 3.

have reached ~8.5 nm, decahedra become thermodynamically preferred, even though they are not as kinetically stable. However, even after long time periods, the fcc structures never gain stability.

This can be understood when we consider the change in shape, as well as the change in size, over time. In Figure 9b, we see a comparison between the observed (kinetic) shapes and the ideal (thermodynamic) shapes, $\Delta G = G(\text{thermo}) - G(\text{kinetic})$. In each case, there is a rapid departure from equilibrium at the early stages of growth, followed by convergence during the steady-state period. The stability of the decahedra improves over time, since the kinetic and thermodynamic shapes are reasonably close. In contrast to the equilibrium fcc shapes predicted by the phase diagram, the kinetic fcc shapes are too far from equilibrium, and they converge to a higher energy shape (by ~2 kJ/mol). We may conclude that the fcc shapes are infrequently observed, even at the thermodynamically preferred sizes, due to an energetic penalty associated with the significant departure from the thermodynamically preferred shape.

Conclusions

Thermodynamic cartography is, at this stage, an emerging technique that offers a simple framework for simultaneously incorporating many important physical variables. It is easy to implement and parametrizable using *ab initio* electronic structure methods, as we have seen here for nanogold. In this Account, a complementary surface area limited kinetic theory of nanomorphology has also been used to explore the temporal size and shape evolution of the same gold nanoparticles. The combined results confirm that gold icosahedra coarsen more quickly and are therefore kinetically more stable, decahedra emerge due to a collaboration between kinetics and thermodynamics, and the infrequent observation of the fcc shapes is governed by thermodynamics alone.

In general, there is a delicate balance between kinetics and thermodynamics during the formation of nanomaterials, and although there is still much to learn, the ability to plot the free energy of faceted morphologies as a function of time will undoubtedly offer new insights in the future.

This project has been supported by the Australian Research Council under Grant Number DP0986752. Computational resources for this project have been supplied by the National Computing Infrastructure (NCI) national facility under MAS Grant p00.

BIOGRAPHICAL INFORMATION

Dr. Amanda Barnard is a theoretical condensed matter physicist, Australian research Council QEII Fellow, and Leader of the Virtual Nanoscience Laboratory at Australia's national science agency, CSIRO. Her research focuses on the nanomaterials structure prediction, and the development of structure/property relationships. For her work, she has been awarded (among others) the IUPAP Young Scientist Prize in Computational Physics (2009), the Australian Prime Minister's prize for Physical Scientist of the Year (2009), and the Frederick White Prize from the Australian Academy of Science for research of intrinsic scientific merit that has an actual or potential contribution to community interests (2010).

FOOTNOTES

*E-mail: amanda.barnard@csiro.au.
The authors declare no competing financial interest.

REFERENCES

1 Daniel, M. C.; Astruc, D. Gold Nanoparticles: Assembly, Supramolecular Chemistry, Quantum-Size-Related Properties, and Applications toward Biology, Catalysis, and Nanotechnology. *Chem. Rev.* **2004**, *104*, 293–346.

2 Campbell, C. T. The Active Site in Nanoparticle Gold Catalysis. *Science* **2004**, *306*, 234–235.

3 Ishida, T.; Haruta, M. Gold Catalysts: Towards Sustainable Chemistry. *Angew. Chem., Int. Ed.* **2007**, *46*, 7154–7156.

4 Gorin, D. J.; Toste, F. D. Relativistic Effects in Homogeneous Gold Catalysis. *Nature* **2007**, *446*, 395–403.

5 Sperling, R. A.; Rivera Gil, P.; Zhang, F.; Zanella, M.; Parak, W. J. Biological Applications of Gold Nanoparticles. *Chem. Soc. Rev.* **2008**, *37*, 1896–1908.

6 Mirkin, C. A.; Letsinger, R. L.; Mucic, R. C.; Storhoff, J. J. A DNA-Based Method for Rationally Assembling Nanoparticles into Macroscopic Materials. *Nature* **1996**, *382*, 607–609.

7 Njoki, P. N.; Lim, I. S.; Mott, D.; Park, H.-Y.; Khan, B.; Mishra, S.; Sujakumar, R.; Luo, J.; Zhong, C.-J. Size Correlation of Optical and Spectroscopic Properties for Gold Nanoparticles. *J. Phys. Chem. C* **2007**, *111*, 14664–14669.

8 Orendorff, C. J.; Sau, T. K.; Murphy, C. J. Shape-Dependent Plasmon-Resonant Gold Nanoparticles. *Small* **2006**, *2*, 636–639.

9 Chithrani, B. D.; Ghazani, A. A.; Chan, W. C. W. Determining the Size and Shape Dependence of Gold Nanoparticle Uptake into Mammalian Cells. *Nano Lett.* **2006**, *6*, 662–668.

10 El-Brolossy, T. A.; Abdallah, T.; Mohamed, M. B.; Abdallah, S.; Easawi, K.; Negm, S.; Talaat, H. Shape and Size Dependence of the Surface Plasmon Resonance of Gold Nanoparticles Studied by Photoacoustic Technique. *Eur. Phys. J. Spec. Top.* **2008**, *153*, 361–364.

11 Dykman, L.; Khlebtov, N. Gold Nanoparticles in Biomedical Applications: Recent Advances and Perspectives. *Chem. Soc. Rev.* **2012**, *41*, 2256–2282.

12 Buffat, P.-A.; Fluëli, M.; Spycher, R.; Stadelmann, P.; Borel, J.-P. Crystallographic Structure of Small Gold Garticles Studied by High-resolution Electron Microscopy. *Faraday Discuss.* **1991**, *92*, 173–187.

13 Marks, L. D. Experimental Studies of Small Particle Structures. *Rep. Prog. Phys.* **1994**, *57*, 603–649.

14 Elechiguerra, J. L.; Reyes-Gasga, J.; José-Yacamán, M. The Role of Twinning in Shape Evolution of Anisotropic Noble Metal Nanostructures. *J. Mater. Chem.* **2006**, *16*, 3906–3919.

15 Bovin, J.-O.; Malm, J.-O. Atoms, Molecules and Clusters. *Z. Phys. D* **1991**, *19*, 293–298.

16 Whetten, R. L.; Khoury, J. T.; Alvarez, M. M.; Murthy, S.; Vezmar, I.; Wang, Z. L.; Stephens, P. W.; Cleveland, C. L.; Luedtke, W. D.; Landman, U. Nanocrystal Gold Molecules. *Adv. Mater.* **1996**, *8*, 428–433.

17 Page, K.; Proffen, T.; Terrones, H.; Terrones, M.; Lee, L.; Yang, Y.; Stemmer, S.; Seshadri, R.; Cheetham, A. K. Direct Observation of the Structure of Gold Nanoparticles by Total Scattering Powder Neutron Diffraction. *Chem. Phys. Lett.* **2004**, *393*, 385–388.

18 Pinto, A.; Pennisi, A. R.; Faraci, G.; D'Agostino, G.; Mobilio, S.; Boscherini, F. Evidence for Truncated Octahedral Structures in Supported Gold Clusters. *Phys. Rev. B* **1995**, *51*, 5315–5321.

19 Seyed-Razavi, A; Snook, I. K.; Barnard, A. S. Origin of Nanomorphology: Does a Complete Theory of Nanoparticle Evolution Exist? *J. Mater. Chem.* **2010**, *20*, 416–421.

20 Pyykkö, P. Relativistic Eeffects in Structural Chemistry. *Chem. Rev.* **1988**, *88*, 563–594.

21 Pyykkö, P. Theoretical Chemistry of Gold. *Angew. Chem.* **2004**, *34*, 4412–4456.

22 José-Yacamán, M.; Herrera, R.; Gómez, A.; Tehuacanero, S.; Schabes-Retchkiman, P. Decagonal and Hexagonal Structures in Small Gold Particles. *Surf. Sci.* **1990**, *237*, 248–256.

23 Cleveland, C.; LuedtkeW., D.; Landman, U. Melting of Gold Clusters: Icosahedral Precursors. *Phys. Rev. Lett.* **1998**, *81*, 2036–2039.

24 Cleveland, C. L.; Landman, U.; Schaaff, T. G.; Shafigullin, M. N.; Stephens, P. W.; Whetten, R. L. Structural Evolution of Smaller Gold Nanocrystals: The Truncated Decahedral Motif. *Phys. Rev. Lett.* **1997**, *79*, 1873–1876.

25 Nam, H.-S.; Hwang, N. M.; Yu, B. D.; Yoon, J.-K. Formation of an Icosahedral Structure during the Freezing of Gold Nanoclusters: Surface-Induced Mechanism. *Phys. Rev. Lett.* **2002**, *89*, No. 275502.

26 Baletto, F.; Ferrando, R.; Fortunelli, A.; Montalenti, F.; Mottet, C. Crossover among Structural Motifs in Transition and Noble-Metal Clusters. *J. Chem. Phys.* **2002**, *116*, 3856–3863.

27 Häberlen, O. A.; Chung, S.-C.; Stener, M.; Rösch, N. From Clusters to Bulk. A Relativistic Density Functional Investigation on a Series of Gold Clusters Au_n, n = 6...147. *J. Chem. Phys.* **1997**, *106*, 5189–5201.

28 Wang, J. L.; Wang, G. H.; Zhao, J. J. Density-Functional Study of Au_n(n = 2−20) Clusters: Lowest-Energy Structures and Electronic Properties. *Phys. Rev. B* **2002**, *66*, No. 035418.

29 Gilb, S.; Weis, P.; Furche, F.; Ahlrichs, R.; Kappes, M. M. Structures of Small Gold Cluster Cations (Au_n^+, n < 14): Ion mobility Measurements versus Density Functional Calculations. *J. Chem. Phys.* **2002**, *116*, 4094–4101.

30 Iijima, S.; Ichihashi, T. Structural Instability of Ultrafine Particles of Metals. *Phys. Rev. Lett.* **1996**, *56*, 616–619.

31 Barnard, A. S.; Curtiss, L. A. Predicting the Shape and Structure of Face Centered Cubic Gold Nanocrystals Smaller than 3 nm. *ChemPhysChem* **2006**, *7*, 1544–1553.

32 Barnard, A. S. Modelling of Nanoparticles: Approaches to Morphology and Evolution. *Rep. Prog. Phys.* **2010**, *73*, 086502–52.

33 Barnard, A. S. Useful Equations for Modeling the Relative Stability of Common Nanoparticle Morphologies. *Comput. Phys. Commun.* **2011**, *182*, 11–13.

34 Barnard, A. S. A Thermodynamic Model for the Shape and Stability of Twinned Nanostructures. *J. Phys. Chem. B* **2006**, *110*, 24498–24504.

35 Guggenheim, E. A. *Thermodynamics*, 4th ed.; North Holland: Amsterdam, 1993.

36 Grosse, A. V. The Relationship between the Surface Tensions and Energies of Liquid Metals and Their Critical Temperatures. *J. Inorg. Nucl. Chem.* **1962**, *24*, 147–156.

37 Qi, W. H.; Wang, M. P. Size and Shape Dependent Melting Temperature of Metallic Nanoparticles. *Mater. Chem. Phys.* **2004**, *88*, 280–284.

38 Barnard, A. S.; Lin, X. M.; Curtiss, L. A. Equilibrium Morphology of Face Centered Cubic Gold Nanoparticles >3 nm, and the Shape Changes Induced by Temperature. *J. Phys. Chem. B* **2005**, *109*, 24465–24472.

39 P. Pawlow, P. Über die Abhängigkeit des Schmelzpunktes von der Oberflächenenergie eines Festen Körpers. *Z. Phys. Chem.* **1909**, *65*, 1–35.

40 Buffat, P.; Borel, J.-P. Size Effect on the Melting Temperature of Gold Particles. *Phys. Rev. A* **1976**, *13*, 2287–2298.

41 Barnard, A. S.; Young, N.; Kirkland, A. I.; van Huis, M. A.; Xu, H. Nanogold: A Quantitative Phase Map. *ACS Nano* **2009**, *3*, 1431–1436.

42 Kuo, C.-L.; Clancy, P. Melting and Freezing Characteristics and Structural Properties of Supported and Unsupported Gold Nanoclusters. *J. Phys. Chem. B* **2005**, *109*, 13743–13754.

43 Koga, K.; Ikeshoji, T.; Sugawara, K. Size- and Temperature-Dependent Structural Transitions in Gold Nanoparticles. *Phys. Rev. Lett.* **2004**, *92*, No. 115507.

44 Koga, K.; Sugawara, K. P. Population Statistics of Gold Nanoparticle Morphologies: Direct Determination by HREM Observations. *Surf. Sci.* **2003**, *529*, 23–35.

45 Yan, H.; Cingarapu, S.; Klabunde, K J.; Chakrabarti, A.; Sorensen, C. M. Nucleation of Gold Nanoparticle Superclusters from Solution. *Phys. Rev. Lett.* **2009**, *102*, No. 095501.

46 Moroni, D.; tenWolde, P. R.; Bolhuis, P. G. Interplay between Structure and Size in a Critical Crystal Nucleus. *Phys. Rev. Lett.* **2005**, *94*, No. 235703.

47 Zhang, T. H.; Liu, X. Y. A kinetic Study Based on Colloidal Crystallization. *J. Phys. Chem. B* **2007**, *111*, 14001–14005.

48 Grochola, G.; Russo, S. P.; Snook, I. K. On Morphologies of Gold Nanoparticles Grown from Molecular Dynamics Simulation. *J. Chem. Phys.* **2007**, *126*, No. 164707.

49 Desgranges, C.; Delhommelle, J. Molecular Simulation of the Nucleation and Growth of Gold Nanoparticles. *J. Phys. Chem. C* **2009**, *113*, 3607–3611.

50 Seyed-Razavi, A.; Snook, I. K.; Barnard, A. S. Surface Area Limited Model for Predicting Anisotropic Coarsening of Facetted Nanoparticles. *Cryst. Growth Des.* **2011**, *11*, 158–165.

51 Lifshitz, I. M.; Slyozov, V. The Kinetics of Precipitation from Supersaturated Solid Solutions. *J. Phys. Chem. Solids* **1961**, *19*, 35–50. Wagner, C. Theory of Precipitate Change by Redissolution. *Z. Electrochem.* **1961**, *65*, 581–591.

52 Burton, W. K.; Cabrera, N.; Frank, F. C. The Growth of Crystals and the Equilibrium Structure of their Surfaces. *Philos Trans. R. Soc. London* **1951**, *243*, 299–358.

53 Sugimoto, T. Preparation of Monodispersed Colloidal Particles. *Adv. Colloid Interface Sci.* **1987**, *28*, 65–108.

54 Barnard, A. S.; Chen, Y. Kinetic Modelling of the Shape-Dependent Evolution of Faceted Gold Nanoparticles. *J. Mater. Chem.* **2011**, *21*, 12239–12245.